NASA/TM–1999–208998

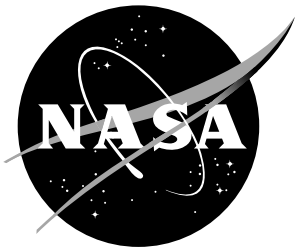

Aerothermodynamic Calculations on X-34 at Mach 6 Wind Tunnel Conditions

William A. Wood
Langley Research Center, Hampton, Virginia

February 1999

The NASA STI Program Office ... in Profile

Since its founding, NASA has been dedicated to the advancement of aeronautics and space science. The NASA Scientific and Technical Information (STI) Program Office plays a key part in helping NASA maintain this important role.

The NASA STI Program Office is operated by Langley Research Center, the lead center for NASA's scientific and technical information. The NASA STI Program Office provides access to the NASA STI Database, the largest collection of aeronautical and space science STI in the world. The Program Office is also NASA's institutional mechanism for disseminating the results of its research and development activities. These results are published by NASA in the NASA STI Report Series, which includes the following report types:

- TECHNICAL PUBLICATION. Reports of completed research or a major significant phase of research that present the results of NASA programs and include extensive data or theoretical analysis. Includes compilations of significant scientific and technical data and information deemed to be of continuing reference value. NASA counterpart and peer-reviewed formal professional papers, but having less stringent limitations on manuscript length and extent of graphic presentations.

- TECHNICAL MEMORANDUM. Scientific and technical findings that are preliminary or of specialized interest, e.g., quick release reports, working papers, and bibliographies that contain minimal annotation. Does not contain extensive analysis.

- CONTRACTOR REPORT. Scientific and technical findings by NASA-sponsored contractors and grantees.

- CONFERENCE PUBLICATION. Collected papers from scientific and technical conferences, symposia, seminars, or other meetings sponsored or co-sponsored by NASA.

- SPECIAL PUBLICATION. Scientific, technical, or historical information from NASA programs, projects, and missions, often concerned with subjects having substantial public interest.

- TECHNICAL TRANSLATION. English-language translations of foreign scientific and technical material pertinent to NASA's mission.

Specialized services that complement the STI Program Office's diverse offerings include creating custom thesauri, building customized databases, organizing and publishing research results... even providing videos.

For more information about the NASA STI Program Office, see the following:

- Access the NASA STI Program Home Page at ***http://www.sti.nasa.gov***

- E-mail your question via the Internet to help@sti.nasa.gov

- Fax your question to the NASA STI Help Desk at (301) 621–0134

- Phone the NASA STI Help Desk at (301) 621–0390

- Write to:
  NASA STI Help Desk
  NASA Center for AeroSpace Information
  7121 Standard Drive
  Hanover, MD 21076–1320

NASA/TM–1999–208998

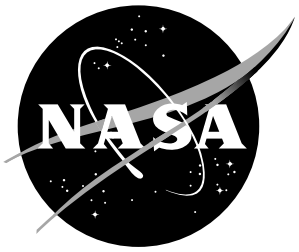

Aerothermodynamic Calculations on X-34 at Mach 6 Wind Tunnel Conditions

William A. Wood
Langley Research Center, Hampton, Virginia

National Aeronautics and
Space Administration

Langley Research Center
Hampton, Virginia 23681–2199

February 1999

Available from:

NASA Center for AeroSpace Information (CASI)
7121 Standard Drive
Hanover, MD 21076–1320
(301) 621–0390

National Technical Information Service (NTIS)
5285 Port Royal Road
Springfield, VA 22161–2171
(703) 605–6000

Abstract

The effects of Reynolds number and turbulence on surface heat-transfer rates are numerically investigated for a 0.015 scale X-34 vehicle at wind tunnel conditions. Laminar heating rates, non-dimensionalized by Fay-Riddell stagnation heating, do not change appreciably with an order of magnitude variation in Reynolds number. Modeling a turbulent versus laminar boundary layer at the same Reynolds number increases the windside heating by a factor of four, portions on the leeside by a factor of two, and causes a 30 percent increase in wing leading edge heating. A discrepancy between laminar and turbulent heating trends on the windside centerline is explained by the presence of attached windside vortices in the laminar solutions, structures that are inhibited by the turbulence modeling.

Nomenclature

C_D	Drag coefficient
C_L	Lift coefficient
C_M	Pitching-moment coefficient
C_P	Pressure coefficient
i, j, k	Streamwise, circumferential, and body-normal computational indices
L/D	Lift-to-drag ratio
M	Mach number
$\bar{Q}$	Nondimensionalized heat-transfer rate
R_e	Reynolds number based on model length
T	Temperature, K
V	Velocity magnitude, m/s
x, y, z	Cartesian coordinates, m
ρ	Density, kg/m^3

Subscripts

∞	Freestream

1 Introduction

X-34[1, 2] is a NASA program with Orbital Sciences Corporation as the prime contractor[3]. The X-34 purpose is to demonstrate next-generation reusable launch vehicle technologies. The X-34 program goals are to build a flight vehicle with first-flight in 1999, demonstrating fully-reusable operation with efficient ground support and quick turn-around times. It is anticipated that a more aircraft-like operational capability will lead to greatly reduced launch costs over current space transportation systems.

The X-34 will be air-launched from an L–1011 airplane. Landing will be on a conventional runway. An artist's sketch of the flight sequence, taken from

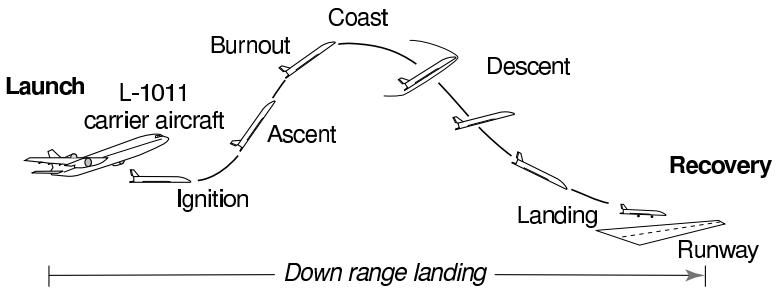

Figure 1: X-34 flight sequence, taken from Ref. [4].

Ref. [4], is depicted in Fig. 1. Flight tests will focus on both low and high-speed performance, with a peak Mach number of 8. Peak heating is expected to occur around Mach 6, with turbulent flow.

NASA Langley has participated in a task agreement with Orbital Sciences to assist in the prediction of the X-34 aerothermodynamic environment and the analysis of the aerothermal design of the vehicle. To this end, a series of wind tunnel experiments and numerical simulations have been performed. Berry *et al*[5] and Merski[6] conducted a matrix of ground-based experimental heating tests using the thermographic phosphor technique at Mach 6 and Mach 10 for both laminar and turbulent flows. Kleb *et al*[4, 7] and Riley *et al*[8] have computed heating rates at flight conditions covering Mach 3–7, with most of the calculations for turbulent flow. Comparisons between the experimental heating data, extrapolated to flight values, and computations has been presented in Refs. [4]–[7].

The present study seeks to provide overlap between the numerical and experimental data sets by performing computational simulations of the X-34 vehicle at wind tunnel conditions. The primary emphasis is on the detailed definition of the thermal environment, though vehicle aerodynamic coefficients and flowfield features are also presented.

2 Configuration

The geometry is a 0.015 scale model of the X-34 outer mold lines, including the thermal protection covering, truncated at the body-flap hinge line. The body flap and rocket nozzle were omitted from the calculations, with an assumed base pressure equal to freestream static pressure. A depiction of the model used in this study is presented in Fig. 2.

The model length is 0.246 m. For convenience, moments are taken about the nose tip, the reference length for aerodynamic coefficients is the model length, and the reference area is the model length squared.

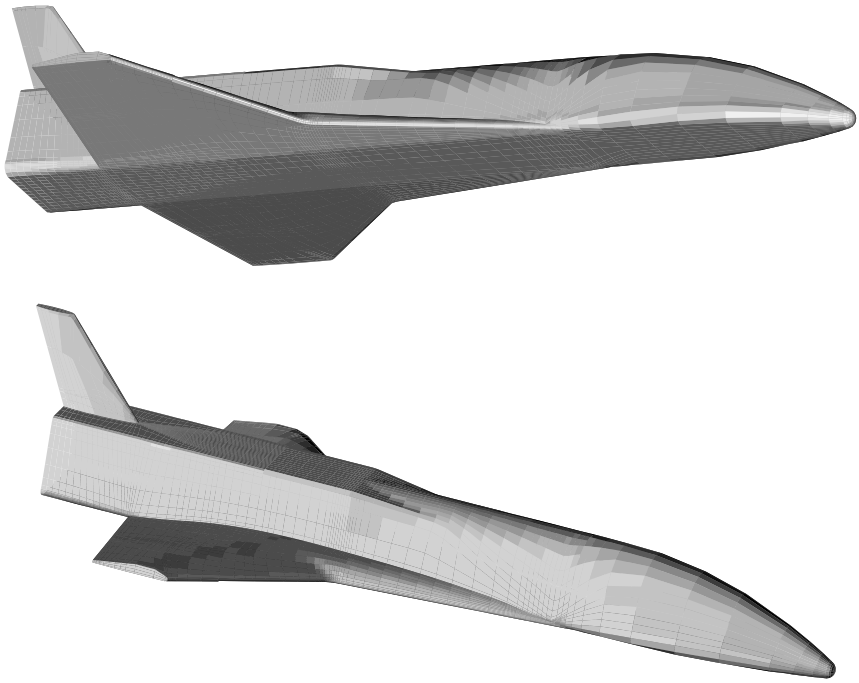

Figure 2: Perspective views of X-34 model.

3 Computational Method

3.1 Solver

Computations were performed using the Langley Aerothermodynamic Upwind Relaxation Algorithm (LAURA)[10, 11, 12]. Perfect-gas air flows were simulated using the upwind-biased, point-implicit scheme for both laminar and turbulent boundary layers.

Thin-layer approximations to the Navier[13]-Stokes[14] viscous terms were applied, retaining only the wall-normal terms in grid blocks adjacent to the vehicle surface. The inclusion of additional viscous terms in the wake of the wing was found to help stabilize and converge the solutions.

The Baldwin-Lomax[15, 16] algebraic Reynolds'-averaged turbulence model was used for the turbulent cases. Fully-turbulent computations, with no transition region, were specified.

LAURA has previously been benchmarked against the Shuttle orbiter[19] at flight conditions, and has been applied to a spectrum of configurations including the X-33[17] and SSV[18] entry vehicles, giving confidence in its predictive capability for the complex hypersonic flows considered here.

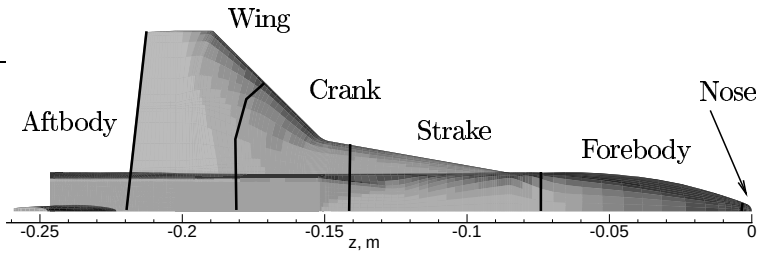

Figure 3: Streamwise blocking for circumferential coarsening.

3.2 Grid

The structured computational mesh contains 369 points in the streamwise direction, 305 points around the vehicle from the windside to leeside symmetry planes, and 65 points normal to the surface. An additional $72 \times 16 \times 80$ grid was inserted behind the wing trailing edge. Details of the grid generation process, including grid-quality assessments, have been reported by Alter[9].

The domain was partitioned into six streamwise blocks, referred to as the nose (i=1–21), forebody (i=21–61), strake (i=61–133), crank (i=133–225), wing (i=225–297), and aftbody (i=297–369). The number of circumferential points, 305, was chosen to resolve all surface features around the wings. Fewer points are needed to resolve the geometrically simpler cross sections forward of the wings. Hence, the strake and crank blocks were coarsened, in the circumferential direction only, by a factor of two, the forebody by a factor of four, and the nose by a factor of eight. A planform view of the configuration with breaklines for the six streamwise blocks is shown in Fig. 3.

The domain was further split into a total of 31 blocks to reduce memory requirements. With this mesh and blocking scheme, the solution required 530 MWords of memory on a 16-processor Cray C-90. Grid adaption was performed to align the mesh with the bow shock and to cluster points in the boundary layer. Solutions required approximately 200 CPU hours each on the C-90.

4 Cases

Two sets of freestream conditions simulate the perfect gas flow of air in a Mach-6 wind tunnel. The core flow is assumed to be uniform.

For the low Reynolds number case: $V_\infty = 927$ m/s, $T_\infty = 60.7$ K, and $\rho_\infty = 0.0160$ kg/m^3. This corresponds to $M_\infty = 5.94$ and $R_e = 0.9 \times 10^6$ based on model length. A laminar solution was computed at these conditions.

For the high Reynolds number case: $V_\infty = 954$ m/s, $T_\infty = 62.4$ K, and $\rho_\infty = 0.1136$ kg/m^3. This corresponds to $M_\infty = 6.02$ and $R_e = 6.4 \times 10^6$. Both laminar and turbulent solutions were computed at these conditions.

The wall temperature is held constant at 300 K and the angle of attack is

$R_e \times 10^{-6}$	Boundary layer	C_D	C_L	C_M	L/D
0.9	laminar	0.003467	0.008280	-0.005813	2.39
6.4	laminar	0.003180	0.008358	-0.005807	2.63
6.4	turbulent	0.003410	0.008472	-0.005932	2.48

Table 1: Aerodynamic coefficients.

15 deg for all cases. Heating results for the high Reynolds number case are normalized by 405 kW/m^2 and for the low Reynolds number case by 128 kW/m^2. These values are determined by a Fay and Riddell[20] stagnation point calculation on a sphere of radius 2.5 mm at the same freestream conditions.

5 Results

5.1 Aerodynamics

To illustrate the effects of Reynolds number and turbulence on the static longitudinal aerodynamic characteristics, lift, drag, and pitching-moment coefficients are presented in Table 1. Recall that the X-34 configuration modeled in this study lacks the aft body flap and bell nozzle present on the true vehicle.

Increasing Reynolds number is seen to reduce C_D and increase C_L, leading to a 10 percent increase in lift-to-drag ratio. Forcing a turbulent boundary layer at the higer Reynolds number further increases C_L by another 1.4 percent, but the 7 percent increase in C_D, leads to an overall 6 percent reduction in L/D.

5.2 Surface Heating

Contour plots of normalized surface heat-transfer rates are presented in Figs. 4–9 for windside, leeside and starboard views. The two laminar solutions, for the low and high Reynolds number cases, are compared side-by-side in Figs. 4–6. Variation of Reynolds number changes neither the contour patterns nor the magnitude of the normalized heating. The only exception is a numerical anomaly in the low Reynolds number case on the fuselage side at the wing-aftbody block boundary, Fig. 6. The localized erratic heating fluctuation at this point is related to a local numerical instability aggravated by very low densities in that region, and is an unreliable representation of the physical heating at that point.

Laminar versus turbulent heating is compared in Figs. 7–9 for the higher Reynolds number case. Windside heating for the turbulent case is as much as four times greater than for the laminar case, though the contour patterns remain largely the same. Turbulent leeside heating, Fig. 8, is about twice as high as laminar heating. The turbulent contours also suggest stronger scrubbing on the leeside fuselage. On the fuselage side, Fig. 9, the turbulent heating on the forebody is about twice the laminar value, but in the middle section of the fuselage both solutions show low heating values. Fuselage heating on the

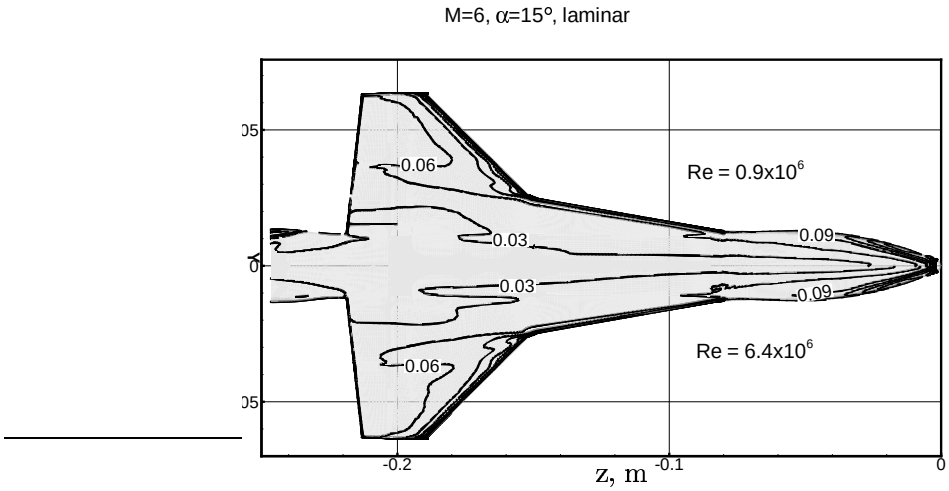

Figure 4: Laminar heat transfer comparison with Reynolds number variation; windside. Contours vary on [0, 0.3] with 0.03 increment.

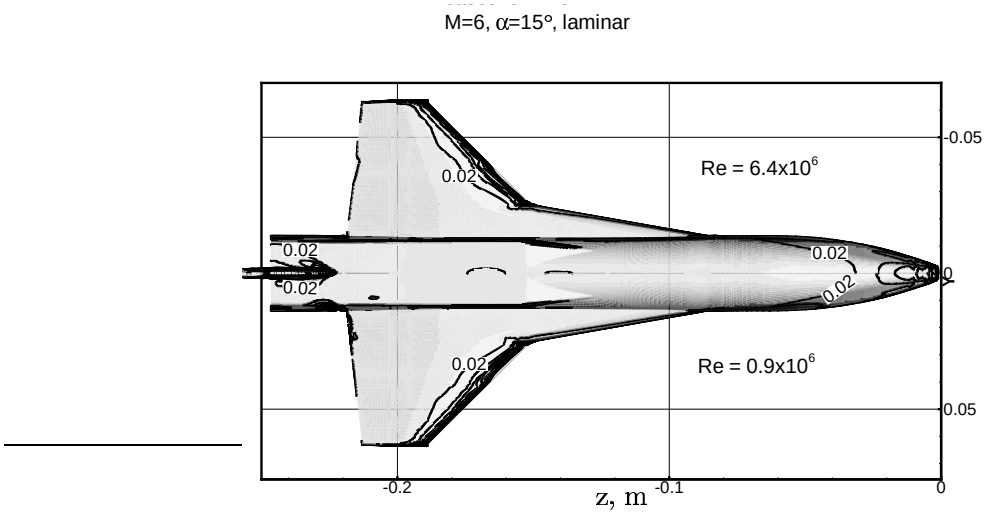

Figure 5: Laminar heat transfer comparison with Reynolds number variation; leeside. Contours vary on [0, 0.2] with 0.02 increment.

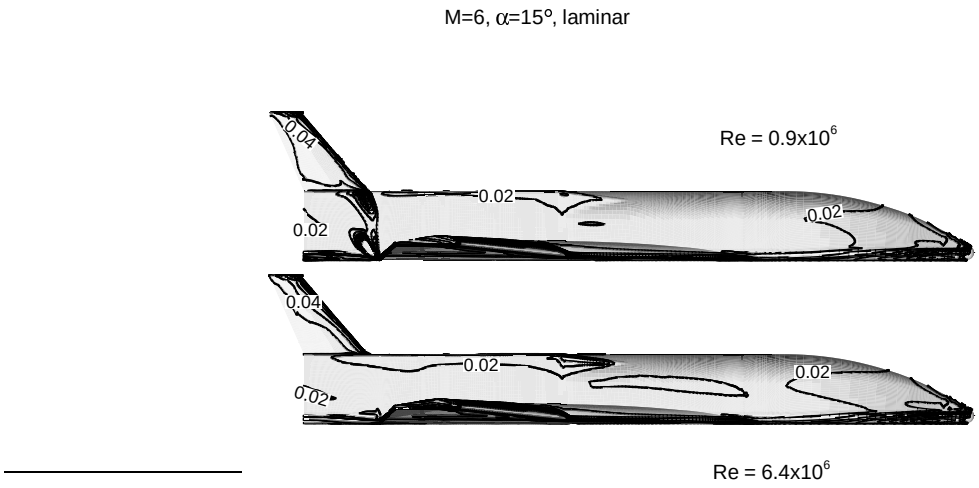

Figure 6: Laminar heat transfer comparison with Reynolds number variation; side. Contours vary on [0, 0.2] with 0.02 increment.

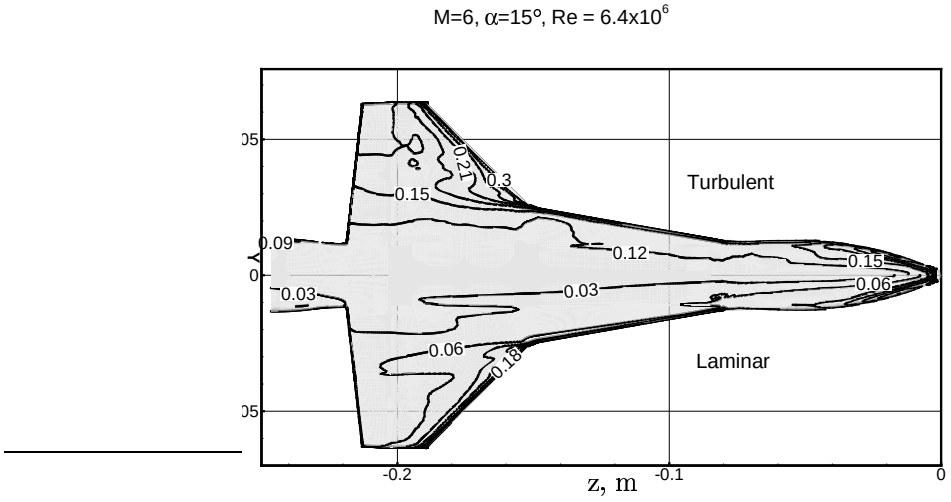

Figure 7: Laminar/turbulent heat transfer comparison; windside. Contours vary on [0, 0.3] with 0.03 increment.

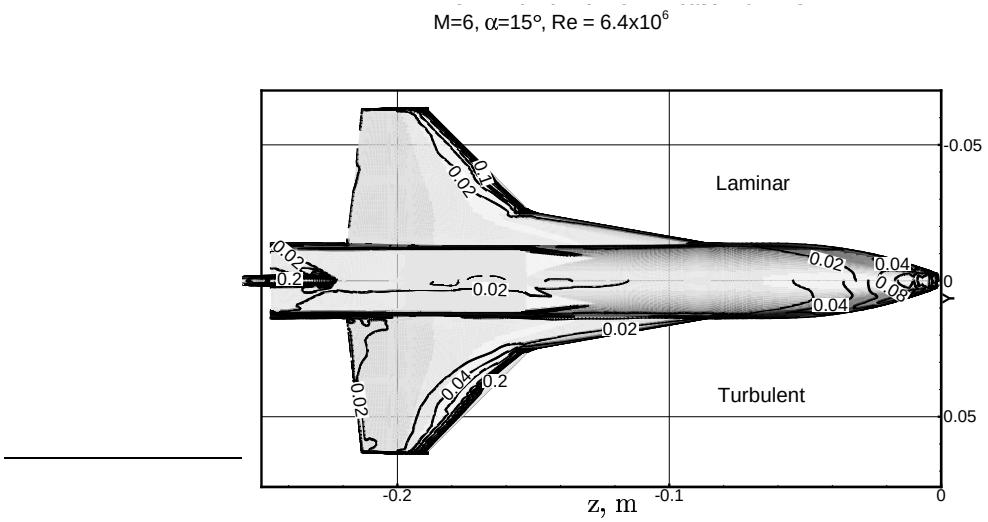

Figure 8: Laminar/turbulent heat transfer comparison; leeside. Contours vary on [0, 0.2] with 0.02 increment.

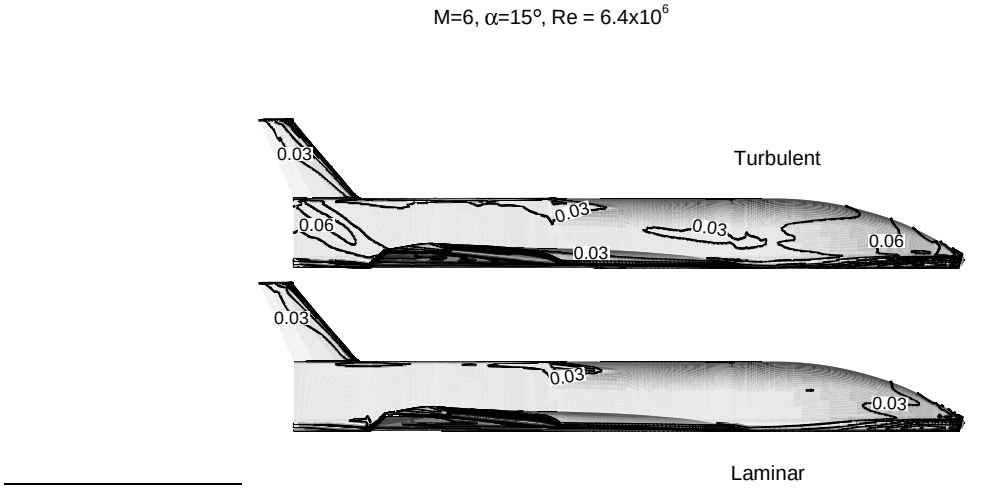

Figure 9: Laminar/turbulent heat transfer comparison; side. Contours vary on [0, 0.3] with 0.03 increment.

aftbody is more than twice as high in the turbulent solution than in the laminar solution, though the contour on the sides of the vertical tail are similar for the two sets of results.

Next, line plots of normalized surface heat-transfer rates are presented, extracted from representative cuts along the vehicle. Windside and leeside centerline heating is shown in Figs. 10 and 11, respectively, for all three cases. Turbulent windside heating is seen to be as much as four times greater than the laminar heating. The effect of turbulence on the leeside centerline produces the most change on the forebody region, where the turbulent heating exceeds the laminar values by more than a factor of two. Increasing the Reynolds number lowers the normalized windside laminar heating between 0–10 percent, but doubles the leeside centerline normalized laminar heating on the rear three-quarters of the vehicle. Normalized heating rates on the vertical tail are similar for all three cases, with the low-Reynolds-number case experiencing some localized numerical difficulties due to extremely high kinetic to internal energy ratio in that region. Both of the laminar solutions show a sudden increase in windside centerline heating at $z = -0.08$ m. This is due to a windside vortex structure, to be discussed in more detail in a following section, upstream of that point. The turbulent solution does not exhibit the same windside vortex structure and subsequent similar heating change there.

Another axial heating plot is shown in Fig. 12. The cut is taken from the nose to the end of the wing tip, following the leading edges of both the strake and the wing. Along the leading edge of the forebody, the turbulent normalized heating is elevated over the laminar values by 50–200 percent. Turbulence has a much smaller effect on the strake leading-edge heating, but then causes about a 30 percent increase in the wing leading-edge heating. Heating along the wing leading edge is seen to be comparable to that at the nose stagnation point.

Normalized heat-transfer rates taken from three cross-sectional slices on the vehicle are presented in Figs. 13–15 versus the x-axis station (positive x points "up" relative to the vehicle). The cuts are from stations $z = -0.03$, -0.13, and -0.16 m. The windside and leeside contour plots of Figs. 7 and 8 can be used to locate these z locations on the vehicle.

The first cross-sectional slice is taken on the forebody at $z = -0.03$ m, Fig. 13. This station corresponds to the location of the windside vortices in the laminar solutions. Figure 13 shows the laminar heating rates drop on the windside by an order of magnitude between the chine and the centerline (left end of the plot). Normalized turbulent heating is 50 percent higher than the laminar values on the chine and twice the laminar values on the leeside.

The second cross-sectional heating cut, Fig. 14, is taken on the strake at $z = -0.13$ m. This station is where the leeside fuselage transitions from a round to rectangular profile. Normalized windside heating distributions for the two laminar solutions are qualitatively similar. The turbulent windside heating is elevated by a factor of three over the laminar values toward the centerline. However, the peak normalized heating on the strake leading edge is comparable for all three cases, at $\bar{Q}$ =0.13–0.18. Laminar heating rates on the side of the fuselage are half the turbulent levels, with the trends suggesting a small separa-

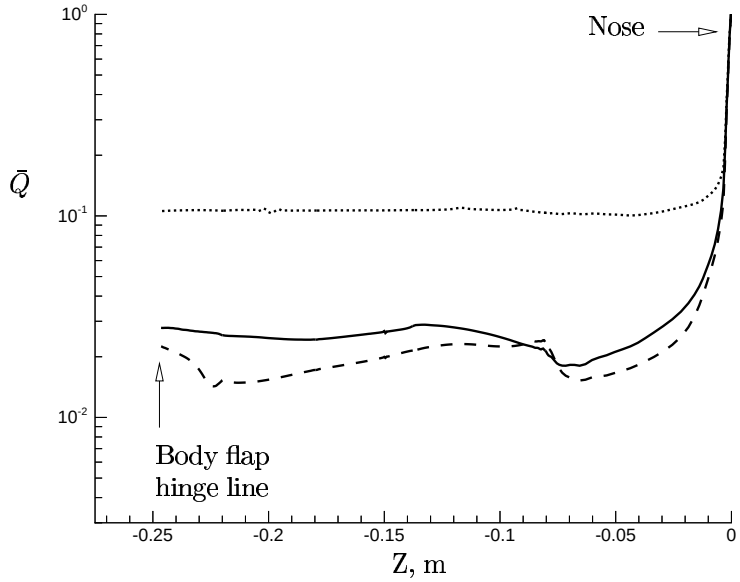

Figure 10: Centerline heat transfer rates; windside. Solid—low R_e. Dashed—high R_e, laminar. Dotted—high R_e, turbulent.

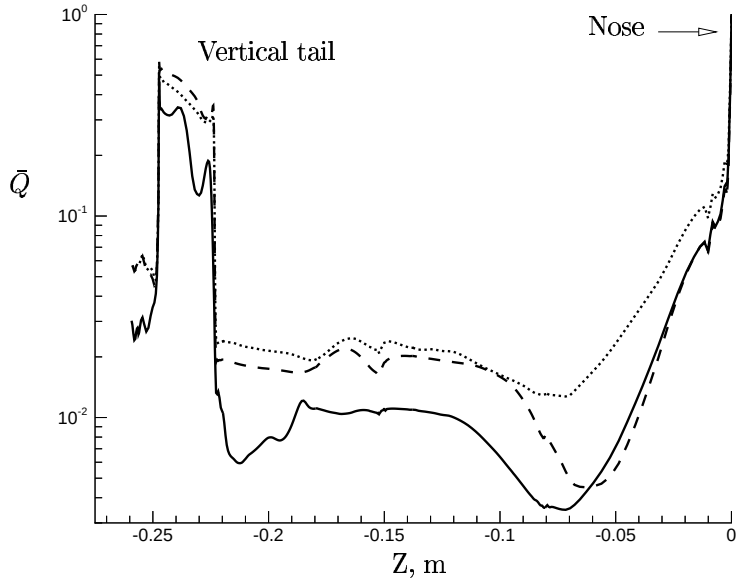

Figure 11: Centerline heat transfer rates; leeside. Solid—low R_e. Dashed—high R_e, laminar. Dotted—high R_e, turbulent.

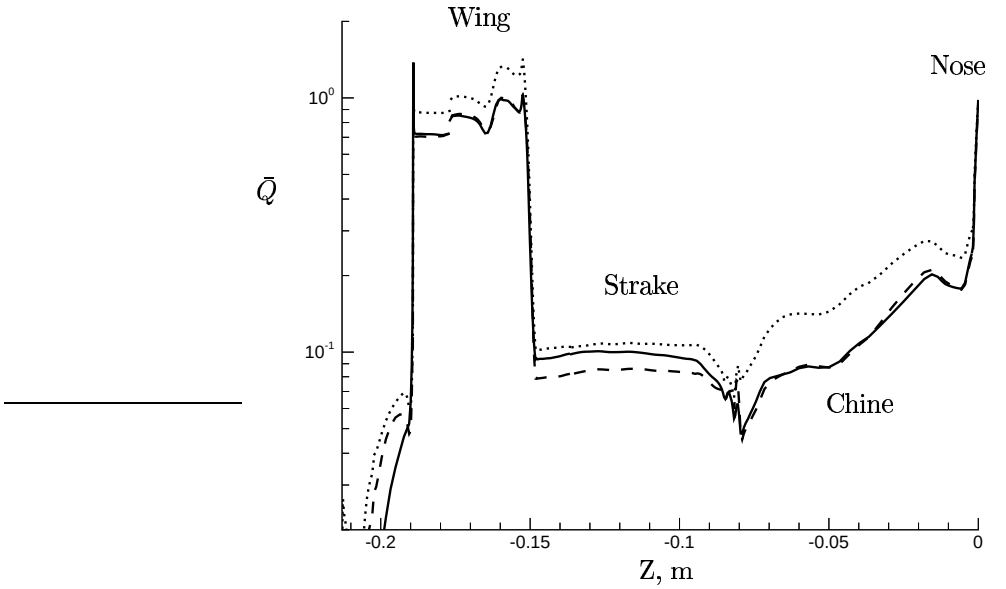

Figure 12: Heat transfer rates along wing leading edge. Solid—low R_e. Dashed—high R_e, laminar. Dotted—high R_e, turbulent.

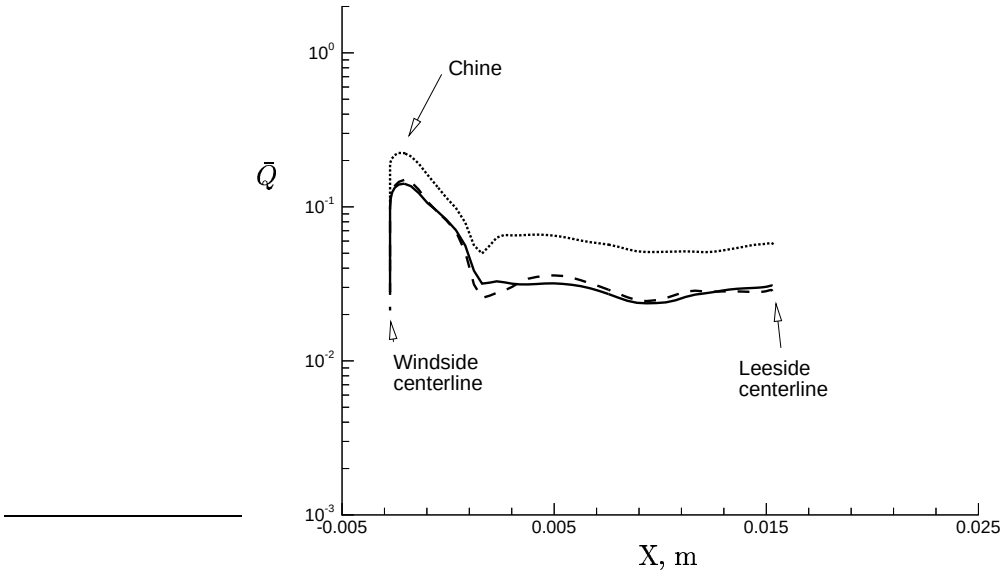

Figure 13: Circumferential heating on forebody, $z = -0.03$ m. Solid—low R_e. Dashed—high R_e, laminar. Dotted—high R_e, turbulent.

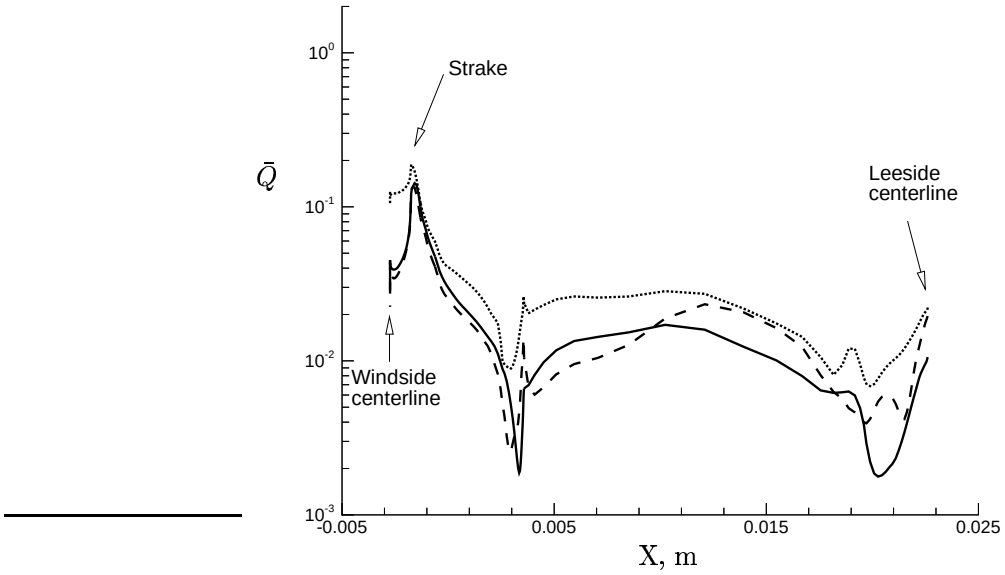

Figure 14: Circumferential heating on strake, $z = -0.13$ m. Solid—low R_e. Dashed—high R_e, laminar. Dotted—high R_e, turbulent.

tion region in the turbulent solution, a separation covering approximately half the fuselage side for the high Reynolds number laminar case, and a separation extending the full height of the fuselage at the lower Reynolds number.

The final cross-sectional heating cut, Fig. 15, is taken through the peak-heating point on the wing leading edge, at $z = -0.16$ m. Turbulent heating is still a factor of three higher than the laminar results on the windside and at least 50 percent higher on the fuselage side. However, there is less difference in the peak heating on the wing leading edge between the laminar and turbulent solutions, at approximately the same value as the nose stagnation-point heating.

5.3 Windside Vortices

A closer look is taken in this section at the generation and decay of windside vortices present on the forebody in the laminar solutions. The location of these vortices coincides with the drop in windside centerline heating seen in Fig. 10. The sudden rise in centerline heating at $z = -0.08$ m, Fig. 10, corresponds with the region where these windside vortices rapidly dissipate.

A sequence of crossflow streamline patterns are shown in Figs. 16–19, taken at $z = -0.002$, -0.01, -0.06, and -0.08 m, respectively. Each of the figures has the same scale, with the focus being on the windside portion of the flowfield. On the spherical nosecap at $z = -0.002$ m, Fig. 16, there is no evidence of crossflow vortices. As the geometry transitions to a triangular cross-section

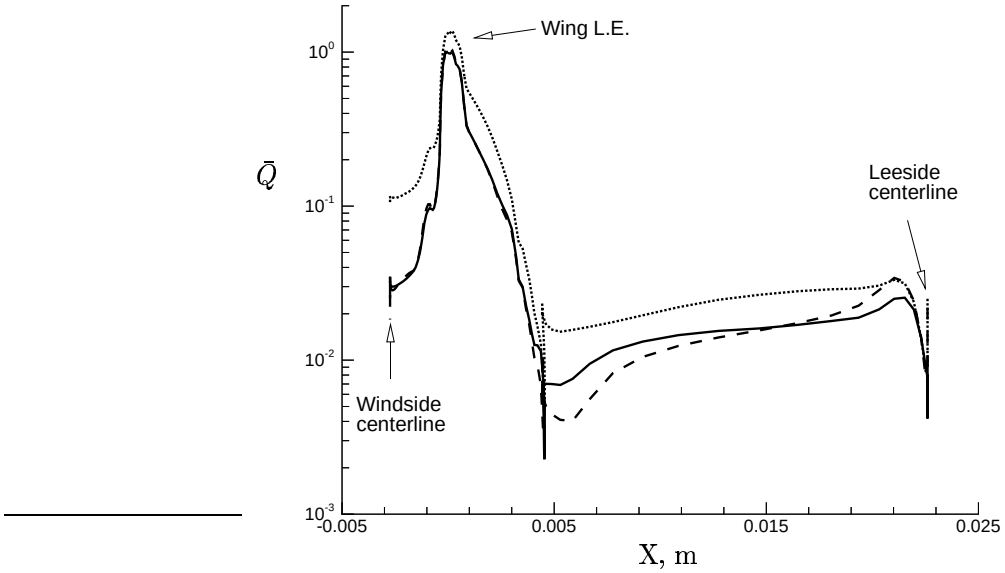

Figure 15: Circumferential heating on wing, $z = -0.16$ m. Solid—low R_e. Dashed—high R_e, laminar. Dotted—high R_e, turbulent.

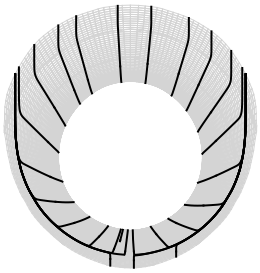

Figure 16: Crossflow streamline patterns at $z = -0.002$ m.

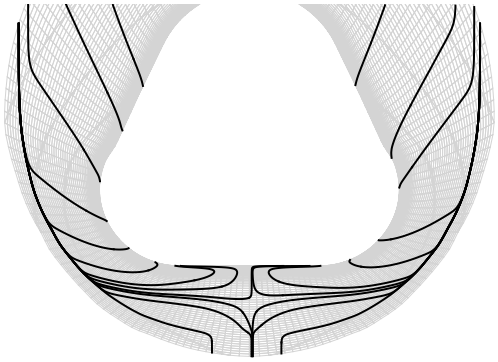

Figure 17: Crossflow streamline patterns at $z = -0.01$ m (windside close-up).

on the forebody, $z = -0.01$ m, Fig. 17, an inboard component develops in the flowfield on the windside, eventually rolling up into a pair of well-defined vortices, Fig. 18. These vortices scrub toward the vehicle centerline, where the streamlines lift off the surface. A little further downstream the vortices dissipate rapidly, as by $z = -0.08$ m, Fig. 19, only a weak circulation remains. Further downstream the circulation is gone, leaving an outboard scrubbing on the windside for the aft three-quarters of the vehicle.

Seeking the source of these windside vortices, pressure coefficient contours in the crossflow plane are shown at two locations. At $z = -0.01$ m, where the vortex structure begins to develop, Fig. 20, the highest pressures are on the chines, with a lower pressure on the windside centerline. This windside inboard pressure gradient, resulting from the change in geometric cross section from circular to triangular, provides the driving potential to establish the vortex formation. Further downstream at $z = -0.08$ m, Fig. 21, the highest pressures are on the windside, with a monotonically decreasing pressure trend toward the chines. The driving potential for the vortical velocity component no longer persists at this point, and viscous damping combined with boundary layer build-up contribute to the dissipation of the vortex pair.

Evidence of boundary layer thickening along the windside centerline of the forebody is shown in Fig. 22, where normalized density contours are presented at $z = -0.06$ m. A bulge of low-density fluid is accumulated at the centerline by the converging, inboard surface shearing. This thickening of the windside centerline boundary layer, created by the windside vortex pattern, coincides with the decreased centerline heating on the forebody in the laminar solutions,Fig. 10.

The turbulent solution, in contrast, exhibits neither a depressed forebody

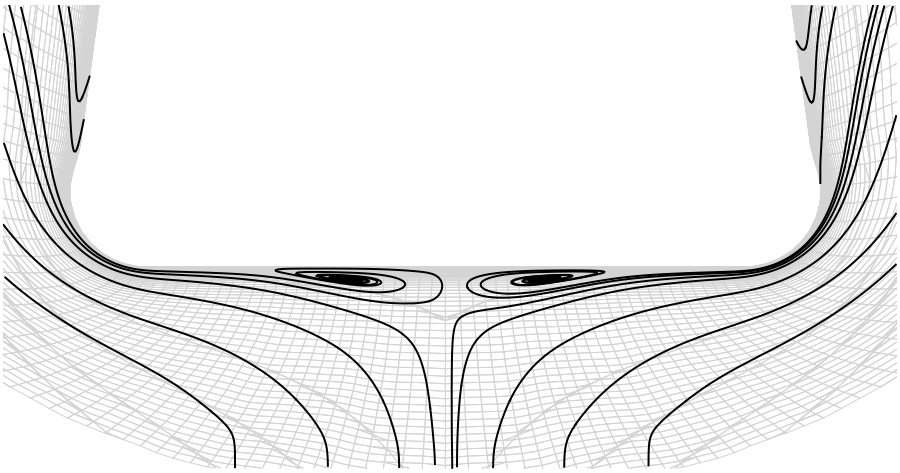

Figure 18: Crossflow streamline patterns at $z = -0.06$ m (windside close-up).

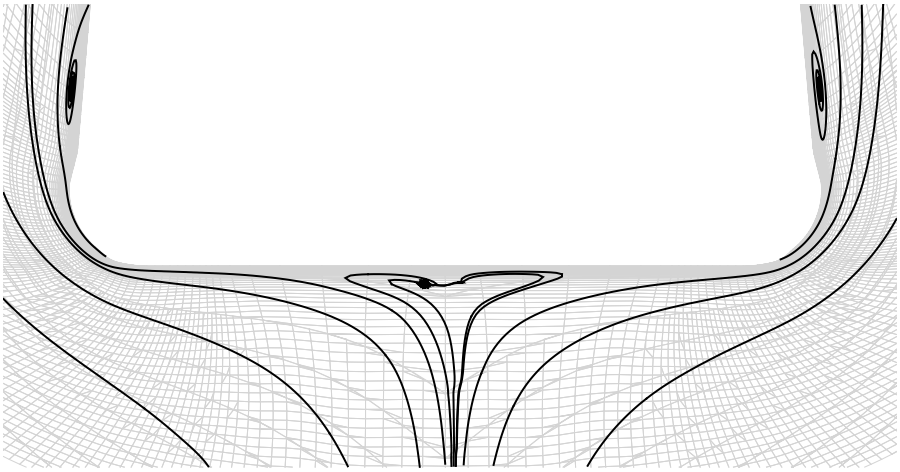

Figure 19: Crossflow streamline patterns at $z = -0.08$ m (windside close-up).

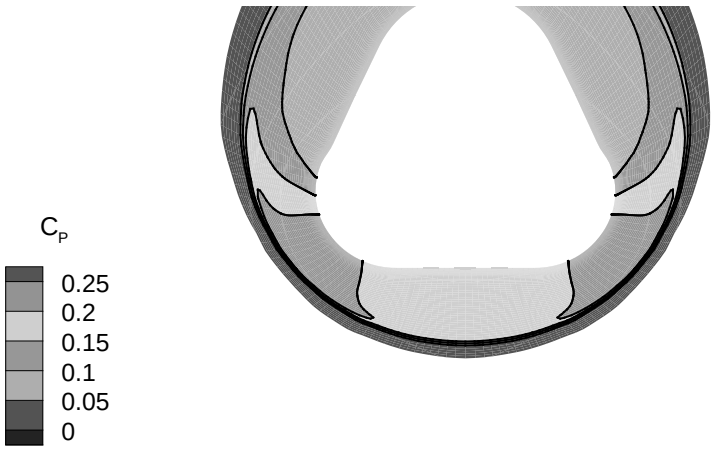

Figure 20: Pressure coefficient in the cross-flow plane at $z = -0.01$ m (windside close-up).

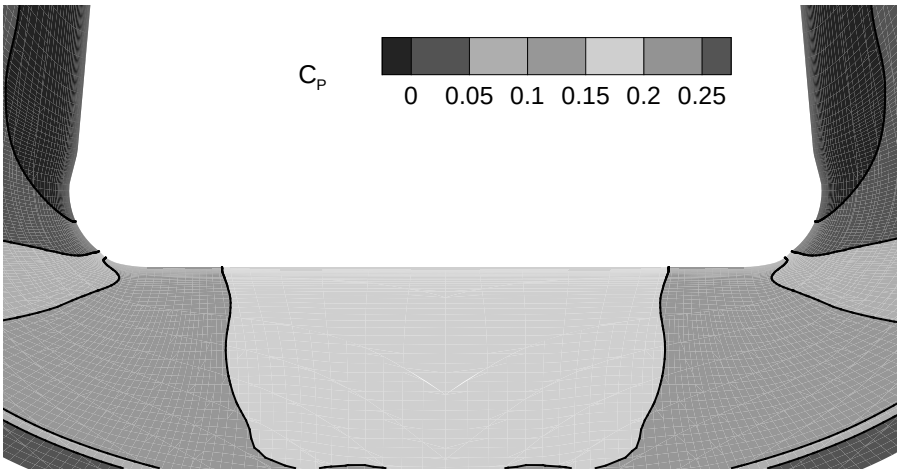

Figure 21: Pressure coefficient in the cross-flow plane at $z = -0.08$ m (windside close-up).

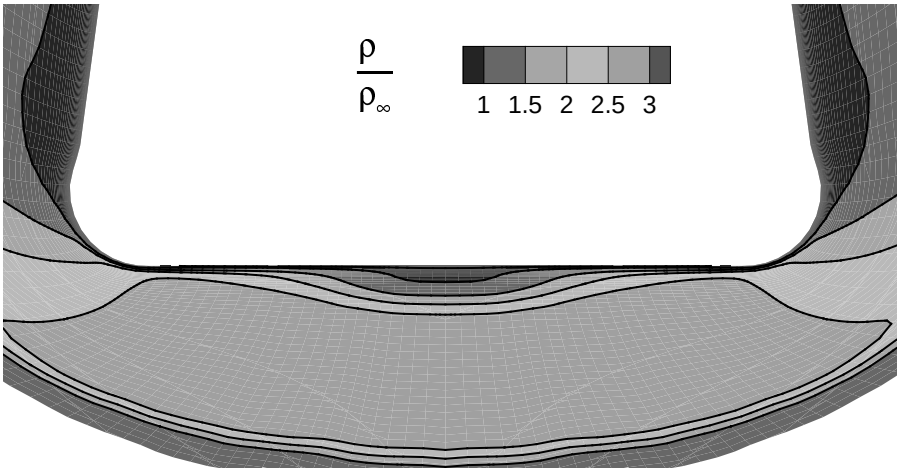

Figure 22: Density contours in the cross-flow plane at $z = -0.06$ m (windside close-up).

centerline heating nor windside vortices on the forebody. The much greater effective boundary layer viscosities for the turbulent case may inhibit the formation of these structures.

6 Summary of Results

A computational study has been performed for the X-34 vehicle (truncated at the body-flap hinge line) at Mach 6 wind tunnel conditions. Two Reynolds numbers are considered, with both laminar and turbulent solutions obtained at the higher Reynolds number.

The effects of Reynolds number variation and turbulence on normalized surface heat-transfer rates are compared using both surface contour plots and extracted-data line plots. Reynolds number variation on laminar solutions has little effect on the normalized windside heating. Some variation in leeside centerline heating is seen between the laminar solutions at different Reynolds numbers.

The increase in heating due to turbulence is seen to vary with location on the vehicle. General trends show windside turbulent heating to be as much as four times greater than laminar heating. On the leeside, the effect of turbulence is most pronounced on the forebody, where heating is elevated by a factor of two. Wing leading edge heating, which is comparable in magnitude to the stagnation point heating, is less effected by turbulence, showing a 30 percent rise over the laminar values.

An abrupt increase in windside centerline heating is indicated for the laminar cases at one-quarter of the vehicle length, unexpected because of the flat,

featureless bottom on the vehicle at that point. Further investigation reveals a pair of windside vortices upstream of the heating rise, generated by the nosecap-to-forebody change in cross section on the vehicle. These vortices dissipate at exactly the same location as the heating increase. The postulation is that these vortices accumulate a thicker windside boundary layer along the centerline over the quarter forebody of the vehicle, locally depressing the centerline heating. As these vortices dissipate, the centerline heating rises to the general value over the whole of the flat windside fuselage. Neither the windside vortices nor a heating change at the quarter forebody location are observed in the turbulent results.

References

[1] Foley, T. M., "Big Hopes for Small Launchers," *Aerospace America*, Vol. 33, No. 7, Jul. 1995, pp. 28–34.

[2] Cook, S. A., "The Reusable Launch Vehicle Technology Program and the X-33 Advanced Technology Demonstrator," NASA TM 111868, Apr. 1995.

[3] NASA, "Reusable Launch Vehicle (RLV), Small Reusable Booster, X-34," Cooperative Agreement Notice CAN 8-2, Jan. 1995.

[4] Kleb, W., Wood, W., Gnoffo, P., and Alter, S. J., "Computational Aeroheating Predictions for X-34," AIAA Paper 98–0879, Jan. 1998.

[5] Berry, S., Horvath, T., DiFulvio, M., Glass, C., and Merski, N. R., "X-34 Experimental Aeroheating at Mach 6 and 10," AIAA Paper 98–0881, Jan. 1998.

[6] Merski, N., "Reduction and Analysis of Phosphor Thermography Data with the IHEAT Software Package," AIAA Paper 98–0712, Jan. 1998.

[7] Kleb, W. L., Wood, W. A., and Gnoffo, P. A., "Computational Aeroheating Predictions for X-34," NASA/TM 1998–206289, USA, Jan. 1998.

[8] Riley, C., Kleb, W., and Alter, S. J., "Aeroheating Predictions for X-34 using an Inviscid-Boundary Layer Method," AIAA Paper 98–0880, Jan. 1998.

[9] Alter, S. J., "Surface Modeling and Grid Generation of Orbital Science's X-34 Vehicle (Phase I)," Contractor Report CR–97–206243, NASA, Nov. 1997.

[10] Cheatwood, F. M. and Gnoffo, P. A., "User's Manual for the Langley Aerothermodynamic Upwind Relaxation Algorithm (LAURA)," NASA TM 4674, Apr. 1996.

[11] Gnoffo, P. A., Gupta, R. N., and Shinn, J. L., "Conservation Equations and Physical Models for Hypersonic Air Flows in Thermal and Chemical Nonequilibrium," NASA TP 2867, Feb. 1989.

[12] Gnoffo, P. A., "An Upwind-Biased, Point-Implicit Relaxation Algorithm for Viscous, Compressible Perfect-Gas Flows," NASA TP 2953, February 1990.

[13] Navier, M., "Mémoire sur les lois du Mouvement des Fluides," *Mémoire de l'Académie des Sciences*, Vol. 6, 1827, pp. 389.

[14] Stokes, G. G., "On the Theories of the Internal Friction of Fluids in Motion," *Trans. Cambridge Philosophical Society*, Vol. 8, 1849, pp. 227–319.

[15] Baldwin, B. S. and Lomax, H., "Thin Layer Approximation and Algebraic Model for Separated Turbulent Flows," AIAA Paper 78–257, January 1978.

[16] Cheatwood, F. M. and Thompson, R. A., "The Addition of Algebraic Turbulence Modeling to Program LAURA," NASA TM 107758, April 1993.

[17] Gnoffo, P. A., Weilmuenster, K. J., Hamilton, H. H., Olynick, D. R., and Venkatapathy, E., "Computational Aerothermodynamic Design Issues for Hypersonic Vehicles," AIAA Paper 97–2473, Jun. 1997.

[18] Weilmuenster, K. J., Gnoffo, P. A., Greene, F. A., Riley, C. J., Hamilton, H. H., and Alter, S. J., "Hypersonic Aerodynamic Characteristics of a Proposed Single-Stage-to-Orbit Vehicle," *Journal of Spacecraft and Rockets*, Vol. 33, No. 4, Jul. 1996, pp. 463–469.

[19] Weilmuenster, K. J., Gnoffo, P. A., and Greene, F. A., "Navier-Stokes Simulations of the Shuttle Orbiter Aerodynamic Characteristics with Emphasis on Pitch Trim and Body Flap," AIAA Paper 93–2814, July 1993.

[20] Fay, J. A. and Riddell, F. R., "Theory of Stagnation Point Heat Transfer in Dissociated Air," *Journal of the Aeronautical Sciences*, Vol. 25, No. 2, Feb. 1958, pp. 73–85.

[21] Brauckmann, G. J., "X-34 Vehicle Aerodynamic Characteristics," AIAA Paper 98–2531, Jun. 1998.

REPORT DOCUMENTATION PAGE

Form Approved
OMB No. 0704–0188

Public reporting burden for this collection of information is estimated to average 1 hour per response, including the time for reviewing instructions, searching existing data sources, gathering and maintaining the data needed, and completing and reviewing the collection of information. Send comments regarding this burden estimate or any other aspect of this collection of information, including suggestions for reducing this burden, to Washington Headquarters Services, Directorate for Information Operations and Reports, 1215 Jefferson Davis Highway, Suite 1204, Arlington, VA 22202–4302, and to the Office of Management and Budget, Paperwork Reduction Project (0704–0188), Washington, DC 20503.

1. AGENCY USE ONLY *(Leave blank)*	2. REPORT DATE	3. REPORT TYPE AND DATES COVERED
	February 1999	Technical Memorandum

4. TITLE AND SUBTITLE
Aerothermodynamic Calculations on X-34 at Mach 6 Wind Tunnel Conditions

5. FUNDING NUMBERS
WU 242-80-01-01

6. AUTHOR(S)
William A. Wood

7. PERFORMING ORGANIZATION NAME(S) AND ADDRESS(ES)
NASA Langley Research Center
Hampton, VA 23681–2199

8. PERFORMING ORGANIZATION REPORT NUMBER
L–17794

9. SPONSORING/MONITORING AGENCY NAME(S) AND ADDRESS(ES)
National Aeronautics and Space Administration
Washington, DC 20546–0001

10. SPONSORING/MONITORING AGENCY REPORT NUMBER
NASA/TM–1999–208998

11. SUPPLEMENTARY NOTES

12a. DISTRIBUTION/AVAILABILITY STATEMENT
Unclassified-Unlimited
Subject Category 16,34 Distribution: Standard
Availability: NASA CASI (301) 621–0390

12b. DISTRIBUTION CODE

13. ABSTRACT ***(Maximum 200 words)***
The effects of Reynolds number and turbulence on surface heat-transfer rates are numerically investigated for a 0.015 scale X-34 vehicle at wind tunnel conditions. Laminar heating rates, non-dimensionalized by Fay-Riddell stagnation heating, do not change appreciably with an order of magnitude variation in Reynolds number. Modeling a turbulent versus laminar boundary layer at the same Reynolds number increases the windside heating by a factor of four, portions on the leeside by a factor of two, and causes a 30 percent increase in wing leading edge heating. A discrepancy between laminar and turbulent heating trends on the windside centerline is explained by the presence of attached windside vortices in the laminar solutions, structures that are inhibited by the turbulence modeling.

14. SUBJECT TERMS
X-34, access to space

15. NUMBER OF PAGES
24

16. PRICE CODE
A03

17. SECURITY CLASSIFICATION OF REPORT	18. SECURITY CLASSIFICATION OF THIS PAGE	19. SECURITY CLASSIFICATION OF ABSTRACT	20. LIMITATION OF ABSTRACT
Unclassified	Unclassified	Unclassified	